J. Fluid Mech. (1976), *vol.* 73, *part* 1, *pp.* 77–96
Printed in Great Britain

Solid-particle motion in two-dimensional peristaltic flows

By TIN-KAN HUNG AND THOMAS D. BROWN
Department of Civil Engineering and Biotechnology Program, Carnegie–Mellon University, Pittsburgh, Pennsylvania 15231

(Received 6 May 1975)

Some insight into the mechanism of solid-particle transport by peristalsis is sought experimentally through a two-dimensional model study (§ 2). The peristaltic wave is characterized by a single bolus sweeping by the particle, resulting in oscillatory motion of the particle. Because of fluid–particle interaction and the significant curvature in the wall wave, the peristaltic flow is highly nonlinear and time dependent.

For a neutrally buoyant particle propelled along the axis of the channel by a single bolus, the net particle displacement can be either positive or negative. The instantaneous force acting upon the particle and the resultant particle trajectory are sensitive to the Reynolds number of the flow (§§ 3 and 4). The net forward movement of the particle increases slightly with the particle size but decreases rapidly as the gap width of the bolus increases. The combined dynamic effects of the gap width and Reynolds number on the particle displacement are studied (§ 5). Changes in both the amplitude and the form of the wave have significant effects on particle motion. A decrease in wave amplitude along with an increase in wave speed may lead to a net retrograde particle motion (§ 6). For a non-neutrally buoyant particle, the gravitational effects on particle transport are modelled according to the ratio of the Froude number to the Reynolds number. The interaction of the particle with the wall for this case is also explored (§ 7).

When the centre of the particle is off the longitudinal axis, the particle will undergo rotation as well as translation. Lateral migration of the particle is found to occur in the curvilinear flow region of the bolus, leading to a reduction in the net longitudinal transport (§ 8). The interaction of the curvilinear flow field with the particle is further discussed through comparison of flow patterns around a particle with the corresponding cases without a particle (§ 9).

1. Introduction

Unlike most phenomena commonly encountered in engineering fluid mechanics, peristaltic pumping is characterized by the dynamic interaction of fluid flow with movement of a flexible boundary. The complexity of such an interaction is somewhat similar to that found in flows around the self-propulsion mechanisms of biological organisms (e.g. spermotozoa and fish) and in blood flows through cardiac chambers. In fact, peristaltic pumping is the common mechanism for

urine transport from kidney to bladder, food mixing and motility in the intestine, ejection of semen in male reproductive organs, and egg transport in female fallopian tubes.

Over the past few years, many analytical studies of peristaltic flows have been conducted. Creeping-flow solutions were obtained by Shapiro (1967) and Shapiro, Jaffrin & Weinberg (1969) for cases when the amplitude A of the peristalsis and the mean channel width are negligibly small compared with the wavelength λ. Besides correlating the forward flow with geometrical and kinematic characteristics of the wave, they also pointed out the possibility of trapping and retrograde fluid motion. Exchanging the assumption of small channel width for an assumption of zero mean pressure gradient, Burns & Parks (1967) and Barton & Raynor (1968) also obtained perturbation solutions which are valid for the limiting case of zero Reynolds number. Zien & Ostrach (1970) and Li (1970) analysed the flow for the low Reynolds number case with zero net flow, while Jaffrin (1971) solved the same problem for a two-dimensional case without the constraint of a vanishing net flow rate.

An extensive nonlinear analysis of two-dimensional peristaltic flow with a small amplitude-to-wavelength ratio was reported by Fung & Yih (1968). Their solution was further supported by the experimental evidence of Yin & Fung (1971), who also enriched their contribution with a similar analysis for the axisymmetric counterpart (Yin & Fung 1969). Most of these studies were related to the activities in urodynamics research promoted by Boyarsky *et al.* (1971). Except for the work of Jaffrin (1971) and the creeping-flow solutions of Tong & Vawter (1972), the common feature of all the aforementioned papers is that the results apply only to flows pumped by a train of sinusoidal waves with a large wavelength-to-amplitude ratio (or $\lambda \gg A$). Retrograde fluid motion was demonstrated by some of the pathlines of fluid particles (Shapiro *et al.* 1969) as well as by the temporal mean velocity at a cross-section (Fung & Yih 1968; Yin & Fung 1969; Zien & Ostrach 1970). Clearly, the wavy motion of the boundary does not necessarily produce a unidirectional flow nor a constant instantaneous flow rate through each cross-section if the observer is not travelling with the speed of the peristalsis. It is known that the pumping mechanism is somewhat similar to the use of viscous forces for transport described by Taylor (1951) for the swimming of spermatozoa.

Ureteral bolus motion has been further analysed by Lykoudis & Roos (1970) and by Fung (1971). The former employed lubrication theory to calculate the pressure generated at the collapsed ends of the bolus. The latter succeeded in coupling the Stokes equations with a membrane equation and concluded that the pressure gradient generated by the peristalsis was very small, and thus ineffective in moving any obstructions in the ureter. Past efforts to identify the effects of ureteral obstruction have usually involved models produced by techniques of extraluminal obstruction using ligatures to produce partial or complete ureteral occlusions.

Recently, Kim *et al.* (1970) reported results of experimentally induced colic using dogs. An artificial calculus was inserted into the ureter to a level between the second and fourth lumbar vertebrae. Observations of ureteral peristalsis,

urine flow, hydronephrosis, ureteral dilation and movement of the artificial calculus were made at 5 min intervals initially, and finally on a daily basis.

A simple estimate can be made here of the average displacement of a calculus transported by the passage of a ureteral bolus. As peristaltic contractions occur 2000–10000 times/day (Labay & Boyarsky 1971), the displacement of a small calculus per bolus will be in the range 0·03–0·15 mm if it takes one day to be pumped from the renal pelvis to the bladder. This ineffective transport of the calculus appears to be caused by the small diameter (approximately 2·5 mm) of the bolus and the relatively large speed (about 3 cm/s) of the ureteral peristalsis. Direct surface contact between the calculus and the collapsed ureteral wall (with an irregular star-shaped cross-section) will cause further physiological and fluid-mechanical difficulties in moving the calculus towards the bladder. Such a surface-to-surface contact is attributed to the peristaltic contraction of the ureter and to gravity, which causes the particle to settle on one side of the ureter. Certainly, calculus transport in the ureter is characterized not only by the unsteady two-phase flow processes but also by the changes in the shape and speed of the ureteral peristalsis caused by the presence of the solid particle, especially when it is tightly fitted into the ureter.

Particulate flows without peristaltic wall contractions have been studied extensively by many fluid mechanicians (refer to Happel & Brenner 1965; Goldsmith & Mason 1966). Similar flow processes occur in the microcirculation (Wang & Skalak 1970; Bungay & Brenner 1973; Skalak, Chen & Chien 1973). The dynamic effects of particles on the dilatation of an elastic tube wall were analysed by Lighthill (1968) and Fitz-Gerald (1972). Lighthill also discussed the difference between peristalsis and the wall dilation caused by tightly fitting solid pellets flowing slowly along a distensible tube. For a calculus moving in the ureter, both peristaltic contraction and passive wall dilation are expected to occur. The coupling between these two types of wall motion makes the problem difficult to analyse.

In an attempt to gain some insight into nonlinear peristaltic flow characteristics, the authors have been working on computational and experimental investigations of nonlinear peristaltic flow and particulate flow by peristalsis. For both cases, one might confine his interest to the physiological phenomena while another might prefer to explore some of the intrinsic characteristics of peristaltic pumping and their potential engineering implications. Clearly, a complete analysis of physiological peristaltic flow processes requires the coupling of the fluid motion with the active muscular contraction as well as the passive dilation of the wall. However present knowledge on the contractility of smooth muscle is very limited.

The purpose of this paper is to obtain some qualitative and quantitative insight into motion of a suspended particle due to the passage of a discrete peristaltic wave. A two-dimensional experimental model has been employed to investigate various geometric and dynamic effects on the particle transport. The peristaltic wave is characterized by a finite ratio of the wave amplitude to the wavelength, as opposed to the very small ratios in the ureteral bolus as well as in the aforementioned analyses and experiments on peristaltic pumping. A two-

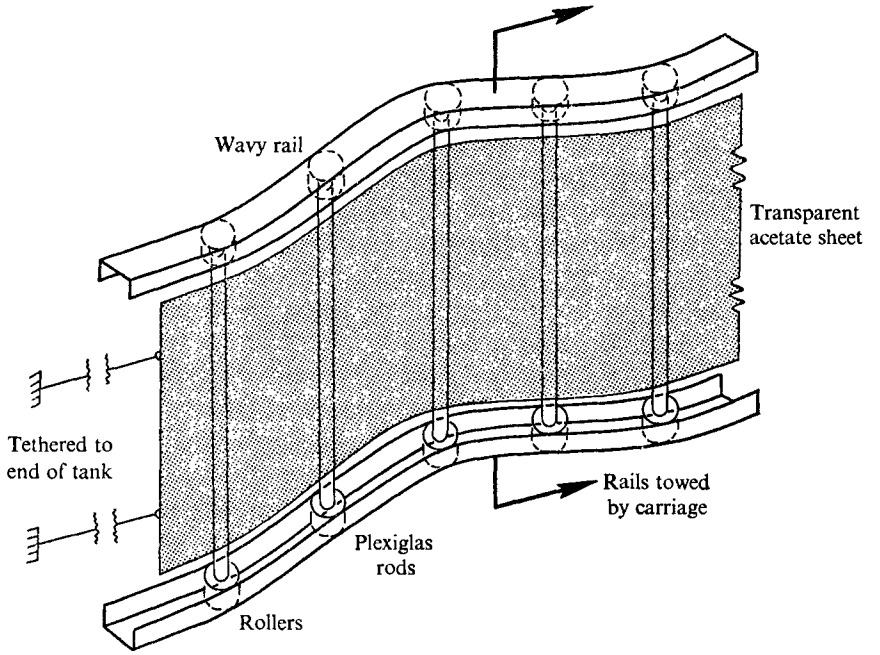

FIGURE 1. Schematic diagram of the method of producing peristaltic waves.

dimensional analysis of peristaltic flow due to segmental wall contraction was recently reported by Lew, Fung & Lowenstein (1971), leading to the exploration of flow characteristics in the intestines. To the authors' knowledge, the present investigation is the first in which the peristaltic flow is highly nonlinear and in which a particle is pumped with the fluid by peristalsis. A study of this two-phase flow process is potentially important in regard both to transport by peristaltic muscular contractions and to the engineering application of pumping solid–fluid mixtures by peristalsis.

2. Experimental apparatus and method

Two-dimensional peristaltic flows were produced between two vertical flexible walls which were submerged in a towing tank (15 ft long, 2·5 ft wide and 3 ft deep) filled with glycerine at the Biological Flows Laboratory of Carnegie–Mellon University. The flexible walls were made of clear acetate sheets (90 in. long, 10 in. high and 15 mils thick) and tethered to the ends of the tank. Plexiglas ribs ($\frac{1}{4}$ in. in diameter and 11 in. long) were attached vertically, at 2 in. intervals, on the outer side of each wall, and rollers ($\frac{5}{8}$ in. in diameter) were fitted to both ends of each rib. Two pairs of horizontal wavy rails were mounted on the carriage of the towing tank and were meshed, respectively, with the top and bottom rollers of each wall (see figure 1). The rails were made of lengths of aluminium extrusion bent into the desired wave forms.

As the rails were towed horizontally by the carriage, the rollers and therefore the ribs, together with the tethered flexible walls, were constrained to follow the

shape of the moving rails, thus generating peristaltic waves. To produce different flows, one could simply change the form of the wavy rails, the spacing between walls, the speed of the moving rails and/or the temperature of the glycerine.

For the study of solid-particle transport, a Plexiglas cylinder (of diameter D and length 9 in.) was suspended vertically in the flow field and adjusted to be neutrally buoyant by attaching small weights to it. In the case of a non-neutrally buoyant particle in a vertically oriented ureteral bolus, the net gravitational force on the solid particle could be simulated by applying a corresponding force on the suspended cylinder. In the present experimental set-up this force would be in the horizontal direction. To satisfy both the Reynolds number $\mathscr{R}$ and Froude number $\mathscr{F}$ critera, the ratio of the magnitude of the gravitational force to that of the viscous force

$$\mathscr{F}/\mathscr{R} = [\rho D^3 g(\rho_s - \rho)/\mu^2]^{\frac{1}{2}} \tag{1}$$

should be preserved (Rouse & Macagno 1966). In (1), ρ and μ are the density and dynamic viscosity of the fluid respectively, g the gravitational acceleration, D the diameter of the particle and ρ_s its density. This density may vary from 1·4 g/cm^3 for a uric-acid calculus to 20 g/cm^3 for calcium oxalate. For the latter, the ratio $\mathscr{F}/\mathscr{R}$ is about 8 when $D = 1$ mm. Surgical intervention is often necessary when D is about 5 mm (Fox, Pyrah & Raper 1965).

Initially, the particle was positioned at a distance (indicated by X_0/λ and Y_0/λ) from the centre of the trailing edge of the stationary bolus. The towing carriage was then accelerated rapidly from rest to a desired speed, and swept by the particle. The peristaltic wave and the motion of the particle were recorded by a 60 frame/s movie camera (Bell & Howell no. 70-DL).

The two-dimensional flow field was visualized by shining a thin sheet of intense light horizontally through the mid-section of the transparent channel walls. Fine air bubbles which were generated when the glycerine was pumped into the towing tank served as tracers for flow observation. Photographs (with time lapse $\leqslant 1$ s) were taken by a camera either mounted at a fixed point or attached to the towing carriage (i.e. moving with the peristaltic wave). The two-dimensional nature of the flow patterns was confirmed by the fact that in the plane of a vertical sheet of light no vertical components of bubble traces were found at all in the central region; only a small three-dimensional effect occurred near the top and bottom of the wavy walls.

Because the wall was inextensible and the ratio A/λ of the wave amplitude to the wavelength was not small, the local wall velocity in the fixed co-ordinates (x, y) of the peristaltic wave had a longitudinal component u as well as a lateral component v, while in the moving co-ordinates (x^*, y^*) these were replaced respectively by

$$u^* = dx^*/dt = d(x - ct)/dt = u - c, \quad v^* = dy^*/dt = v. \tag{2}$$

When the peristaltic wall wave may be described by a sinusoidal function

$$y = y^* = \tfrac{1}{2}d + \tfrac{1}{2}A\{1 + \sin[2\pi x^*/\lambda - \tfrac{1}{2}\pi]\} \quad \text{for} \quad 0 < x^* < \lambda, \tag{3}$$

it corresponds to a single travelling wave with speed c, amplitude A and wavelength λ. The gap width d downstream of the leading edge (refer to section B in

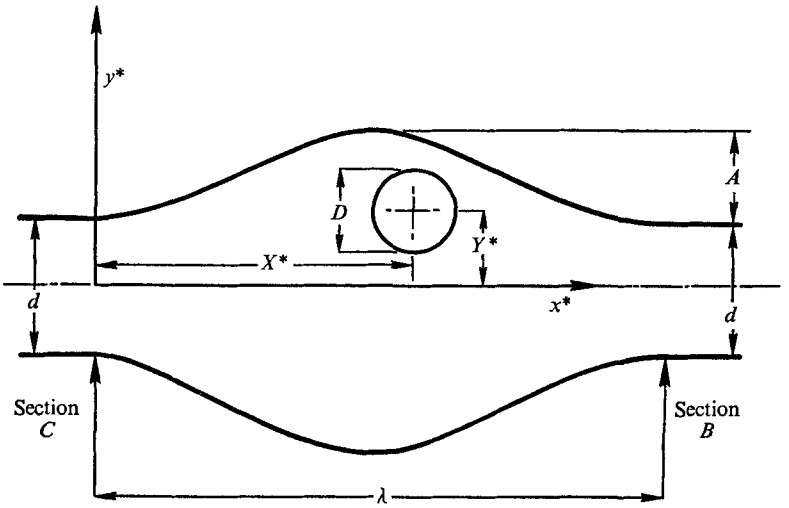

FIGURE 2. Definition of geometric parameters. The wave is moving from left to right.

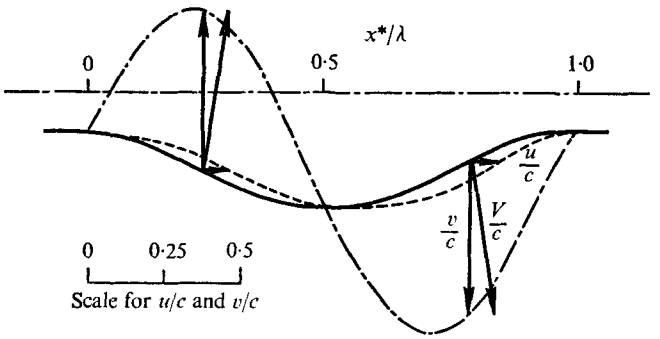

FIGURE 3. Velocity distribution on the wall for wave I.

figure 2) as well as upstream of the trailing edge (section C) was constant. For an infinite train of waves propagating along an inextensible wall, the velocity of the wall can be easily evaluated from the moving co-ordinates using Taylor's method; that is, the velocity is tangential to the wall and has a constant magnitude of $-cS/\lambda$, where S is the arc length along the wavy wall. The trajectory of a point on the wall has the form of a figure of eight. However, this is not the case for a discrete bolus wave, where a point on the wall will have a net forward displacement per peristalsis. A numerical procedure was employed to evaluate the kinematics of the wall wave in the fixed frame with a net longitudinal displacement per wave of $S-\lambda$. Figure 3 shows the form of wave I and the calculated velocity distributions (in the fixed frame) on the wavy wall. Notice that u/c is always positive while the sign of v/c depends on whether the point is on the contracting or dilating segment of the wall.

Four pairs of wavy walls were used in this study. The first three pairs differ from one another only in the wave amplitudes, equal to $0{\cdot}164\lambda$, $0{\cdot}328\lambda$ and $0{\cdot}082\lambda$ respectively. The fourth wave can be considered to be the same as the first except

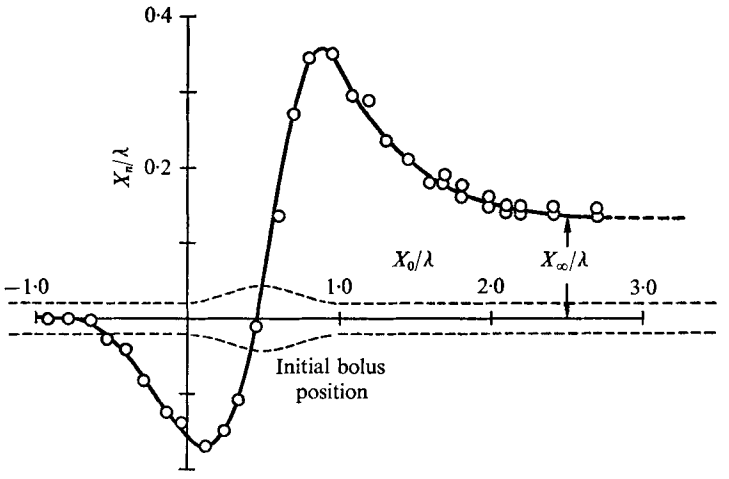

FIGURE 4. Effect of initial particle position on net particle transport per bolus passage. Wave I, $\mathscr{R} = 5{\cdot}96$, $d/\lambda = 0{\cdot}285$, $D/\lambda = 0{\cdot}103$.

that a flat segment of length $0{\cdot}5\lambda$ has been inserted in the middle of the wavy wall. They are referred to hereafter as waves I, II, III and IV. Thus the wavelength λ_{IV} of wave IV is equal to $1{\cdot}5\lambda$, and the velocity distributions on the wavy portions of wave IV are the same as the corresponding ones for wave I (figure 3) except in the middle flat portion of the wave, where $u = v = 0$.

3. Kinematics and dynamics of the particle motion

For a single peristaltic wave of fixed geometry passing over a particle, the net transport distance depends upon the initial particle position (X_0, Y_0). The experimental data show that there is practically no lateral motion or rotation of the particle if it is initially on the longitudinal axis ($Y_0 = 0$). As shown in figure 4, both positive and negative net longitudinal displacements X_n of the particle are possible, and in this case they occur respectively for X_0/λ larger or smaller than $0{\cdot}45$. X_n was measured after the particle returned to rest. The maximum value of X_n was found for X_0/λ slightly smaller than 1. Increasing X_0/λ above 1 leads to an adverse effect on the forward particle transport, and finally an asymptotic value X_∞ of the displacement is reached if $X_0/\lambda > 2{\cdot}5$.

Figure 5 shows the trajectory (X, Y) of the centre of a particle pumped by peristalsis. Initially (i.e. when $ct/\lambda = 0$), the particle is at rest and is located at $X_0/\lambda = 2{\cdot}5$. As the peristaltic wave (wave I) propagates towards it, the particle experiences first a backward motion followed by a forward one, then a backward one again, finally coming to rest at $ct/\lambda = 3{\cdot}7$. The initial retrograde motion is caused by the local backward velocity of fluid at the leading edge, which can be seen from the flow pattern shown in figure 6 (plate 1). The velocity distribution was measured from segments of air-bubble traces. Notice that backward flows occur at both ends of the bolus, with two instantaneous stagnation points dividing the forward flow from the backward flows. The distance between these stagnation

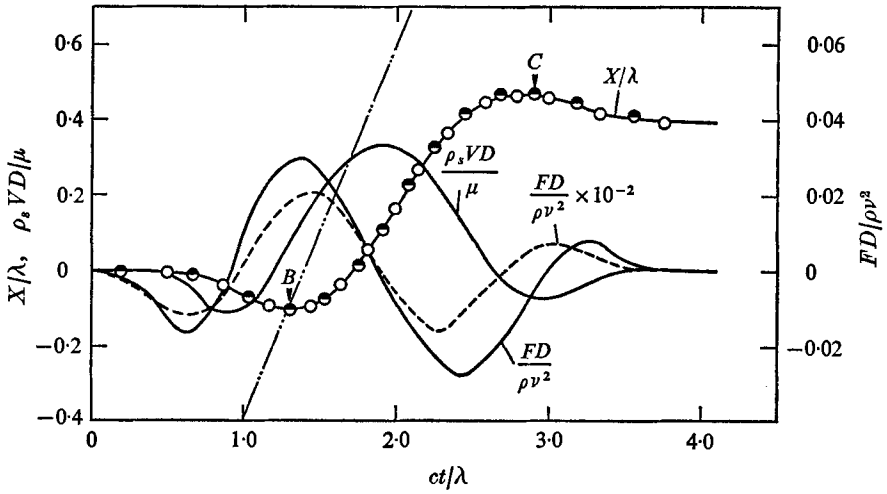

FIGURE 5. Particle displacement, velocity and force. Wave I, $d/\lambda = 0{\cdot}315$, $D/\lambda = 0{\cdot}103$. ——, $\mathscr{R} = cA/\nu = 0{\cdot}84$; ○, $\mathscr{R} = 0{\cdot}84$, $\mu = 10{\cdot}7$ P; ◓, $\mathscr{R} = 0{\cdot}84$, $\mu = 15{\cdot}3$ P; – – –, $\mathscr{R} = 7{\cdot}03$, $\mu = 15{\cdot}3$ P.

points tends to reduce as d decreases and/or as c increases. This retrograde flow may not occur if the leading part of the peristaltic wall motion is passive; that is, if the wall is pushed by the fluid in the bolus rather than by an active (or mechanically produced) dilation of a prescribed form as in the present model. For the former, the shape of the leading part of the wave will be determined by the coupling between the effects of the flow field and the material characteristics of the wall. The straight line in figure 5 represents the trajectory of the leading edge of the peristaltic wave. Proceeding from the lower left, the leading edge of the wave passes the centre of the particle at point B. The trailing edge overtakes the particle when the latter reaches point C. The instantaneous dimensionless particle velocity $\rho_s VD/\mu$ and force on the particle $DF/\rho\nu^2$ (where F is the net force acting on a unit length of the particle and $\nu = \mu/\rho$) may be calculated directly from the time derivatives of the particle trajectory (see sample data points in figure 5). An oscillatory velocity curve and a somewhat skew-symmetric force curve are obtained. In particle fluid dynamics, $DF/\rho\nu^2$ often represents a constant drag force or the force causing particle migration (Happel & Brenner 1965, p. 46). However in this study it oscillates with time and is related to the dimensionless particle velocity by

$$\frac{FD}{\rho\nu^2} = \frac{\pi D^2}{4\nu}\frac{d}{dt}\left[\frac{\rho_s VD}{\rho\nu}\right]. \tag{4}$$

Integration of (4) with respect to time yields

$$X = \int_0^t\int_0^t \frac{1}{M} F\,dt\,dt + \int_0^t V_0\,dt + C_2, \tag{5}$$

where V_0 is the initial particle velocity, $M = \frac{1}{4}\rho_s\pi D^2$ and C_2 is the particle's position at $t = 0$. In order to interpret the mean value of the magnitude of F over

the period T when the particle is moving between the leading and trailing edges of the bolus, a hypothetical constant force F^* resulting in the same net displacement X_b per bolus (i.e. over the same period) is defined. Thus one can obtain from (5)

$$X_b = F^*T^2/2M + V_B T, \tag{6}$$

where V_B is the particle's velocity when the leading edge B passes it. By definition, T can be related to the wave speed, λ and X_b by

$$T = (\lambda + X_b)/c. \tag{7}$$

The calculated mean $|F|$ for $\mathscr{R} = 0{\cdot}84$ over this period for the $FD/\rho\nu^2$ curve shown in figure 5 is found to be 2·7 times larger than the corresponding F^* [refer to (6)]. For higher Reynolds numbers (e.g. $\mathscr{R} = 7{\cdot}03$; see dashed line in figure 5), the ratio of $|F|$ to F^* is found to increase to 5. Worthy of notice is the fact that the net force (or $FD/\rho\nu^2$) can increase by two orders of magnitude when the wave speed (or $\mathscr{R}$) increases by a factor of ten (refer to figure 5).

4. The Reynolds number effects

Clearly the intensity of the peristaltic pumping increases with the velocity components of the wall motion. As expressed by (2) and (3), these velocity components rise with c and A. Also, the wavelength λ of a discrete or of a continuous peristalsis affects the particle displacement. The effects of A/λ on X will be discussed in § 6.

In the published work on peristaltic flows (Shapiro *et al.* 1969; Fung & Yih 1968; Li 1970), there is no general consensus on the choice of the reference length for the definition of the Reynolds number, as each author selects either A, d or A^2/λ to suit his perturbation analysis or creeping-flow solution. In this paper, the characteristic Reynolds number for the peristaltic pumping is defined as cA/ν. The effects of d/A and λ/A and will then be investigated for given values of $\mathscr{R}$.

In the early phase of the experimental study, it was found that the effects of the finite length of the flexible walls could lead to inconsistency in the particle transport when μ and c varied while $\mathscr{R}$ remained constant. This artifact was then effectively eliminated by extending the flexible walls to a length of 7λ. As shown by the various data points in figure 5, different wave speeds which correspond to a large variation in the fluid temperature or viscosity were used to confirm the reproducibility of the particle trajectory for a given $\mathscr{R}$. The reliable range of the wave speeds used in this experimental set-up was found to be from 1 to 9 cm/s. An improper slipping between the rails and the rollers (refer to figure 1) sometimes occurred when the wave speed was extremely low, resulting in an undesirable jerking movement of the peristaltic wave. Small surface waves were observed for $c > 9$ cm/s.

The decrease in the particle transport with increasing Reynolds number can be seen from the series of curves in figure 7. The origin of this figure corresponds to the time and location when the leading edge of the wave passes the centre of the particle (refer to point B in figure 5). The envelope of the trajectories preceding B is shown by the dashed lines at the lower left edge. The increasing slope

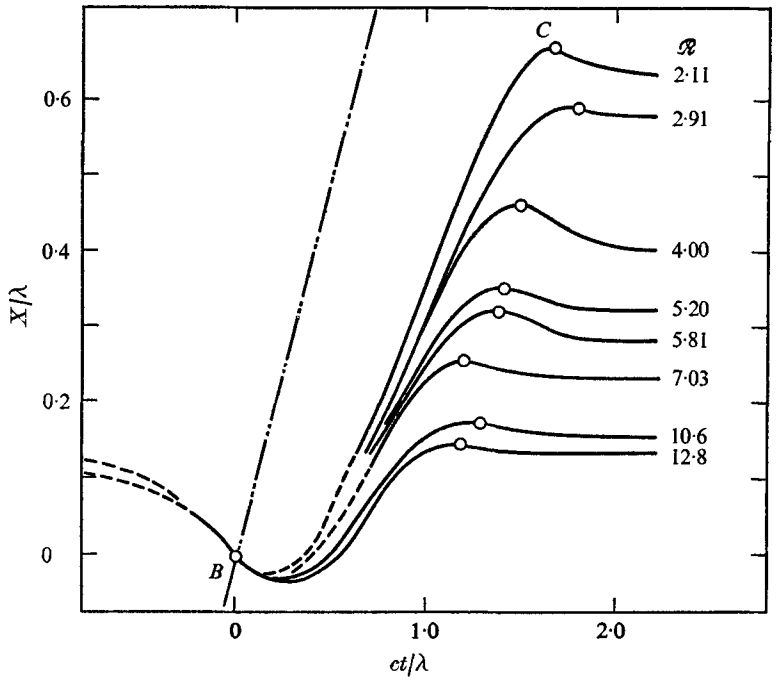

FIGURE 7. Effect of Reynolds number on particle trajectory. Wave I, $d/\lambda = 0{\cdot}285$, $D/\lambda = 0{\cdot}103$.

for a series of forward motions of the particle shows the relative viscous effect of the peristalsis on the particle transport. Notice that for $\mathscr{R} = 12{\cdot}8$ the net particle transport almost vanishes.

As it was impossible to perform an experiment for the creeping-flow case (i.e. $\mathscr{R} \to 0$), an analysis was made to extrapolate the longitudinal particle displacement X_b per passage of a bolus. The ratio of an 'equivalent momentum flux' of the particle to the absolute value of the longitudinal momentum flux through the contracting parts of the bolus is

$$\Phi = \frac{\rho_s D(X_b/T)^2}{2\int_s \rho u \mathbf{V}.\mathbf{n}\, dS}, \tag{8}$$

where $\mathbf{V}$ is the velocity vector and $\mathbf{n}$ the unit normal to the wall. In this expression, X_b/T represents the mean velocity of the particle during the passage of a bolus over the particle:

$$\frac{X_b}{T} = \frac{cX_b}{X_b+\lambda} = c\left[1-\frac{\lambda}{X_b}+\left[\frac{\lambda}{X_b}\right]^2-\left[\frac{\lambda}{X_b}\right]^3+\ldots\right]. \tag{9}$$

As will be shown in the next section, the particle transport increases rapidly with a decrease in d; one may imagine that, for very small d/A, λ/X_b will be very much less than unity for creeping flow ($\mathscr{R} \to 0$). Thus the particle will assume a limiting velocity c. The corresponding limiting value Φ_0 for wave I is 3·7.

From (6) and (7), one can obtain an 'equivalent thrust coefficient'

$$C_T^* = \frac{DF^*}{\rho\nu^2} = \frac{\pi\rho_s}{2\rho_0}\mathscr{R}^2\frac{[X_b - V_0(X_b+\lambda)/c]\,D}{(X_b+\lambda)^2}. \tag{10}$$

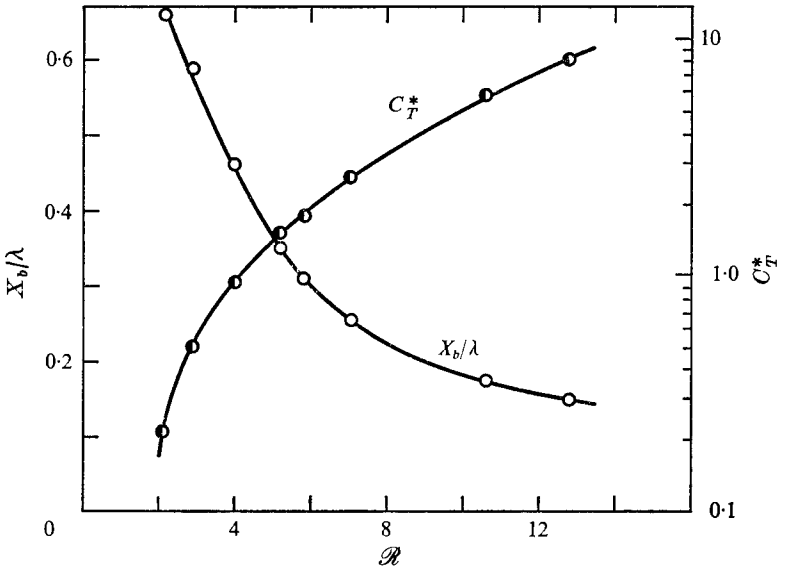

FIGURE 8. Thrust coefficient for wave I. $d/\lambda = 0{\cdot}285$, $D/\lambda = 0{\cdot}103$.

As can be seen in figure 8, C_T^* rises as $\mathscr{R}$ increases while the net particle displacement X_b/λ actually falls. This means that for a given wave form any increases in particle thrust due to an increase in lateral wall velocity or in $\mathscr{R}$ are more than offset by the decreased transport time owing to the corresponding higher wave speed. The pumping effects will be further discussed for changes in the amplitude of the wave.

5. The effects of channel width and particle size

As the peristaltic pumping is primarily based on the intrinsic mechanism of viscous effects, a decrease in the channel width d is expected to result in an increase in the particle transport. Figure 9 shows that, for a particle of given size ($D/\lambda = 0{\cdot}1$) pumped by wave I, a 20 % decrease in d can lead to a several-fold rise in X_∞, depending on the Reynolds number. However, the salient results also indicate that for two channel widths the increment (or difference) in X_∞ is fairly insensitive to $\mathscr{R}$. The scatter of some data is primarily due to a slight deviation of the particle from the axis (i.e. $Y = 0$). For d/λ values larger than those shown in figure 9, one may suspect that X_∞ approaches zero at even smaller $\mathscr{R}$. Experimental data for $\mathscr{R} > 14$ were not taken as they required a high rise in the glycerine temperature or even a change of fluid. The dashed lines in figure 9 reflect a small change in X_∞ caused by a variation in particle size ($D = 0{\cdot}64$–$7{\cdot}9$ cm). As shown in figure 10, a larger ratio D/d of particle size to channel width appears to lead to a larger X_∞/λ. However the effects of D on the particle transport are much smaller than those of d. It should be noted that the data for the solid curves in figure 9 were obtained using one size of particle ($D = 3{\cdot}14$ cm), while the data shown in figure 10 were obtained using seven different particle sizes but one

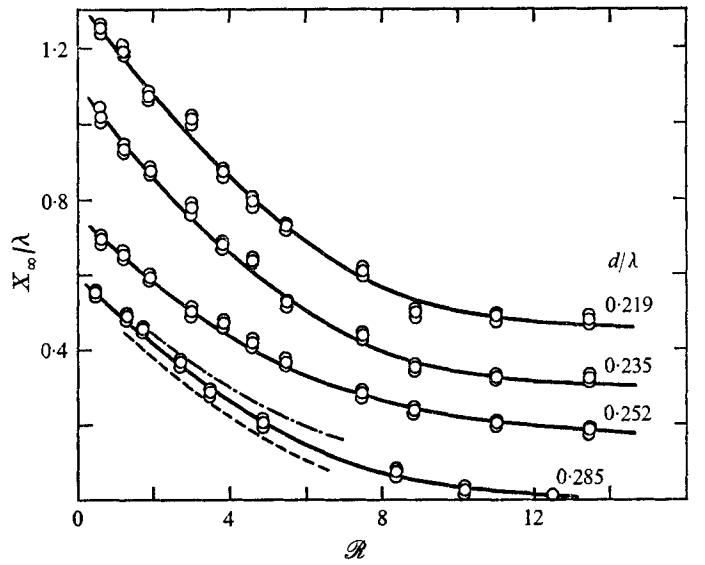

FIGURE 9. Effect of minimum channel width d/λ on net particle transport for wave I. ——, $D/\lambda = 0{\cdot}103$; —·—, $D/\lambda = 0{\cdot}259$; – – – –, $D/\lambda = 0{\cdot}021$.

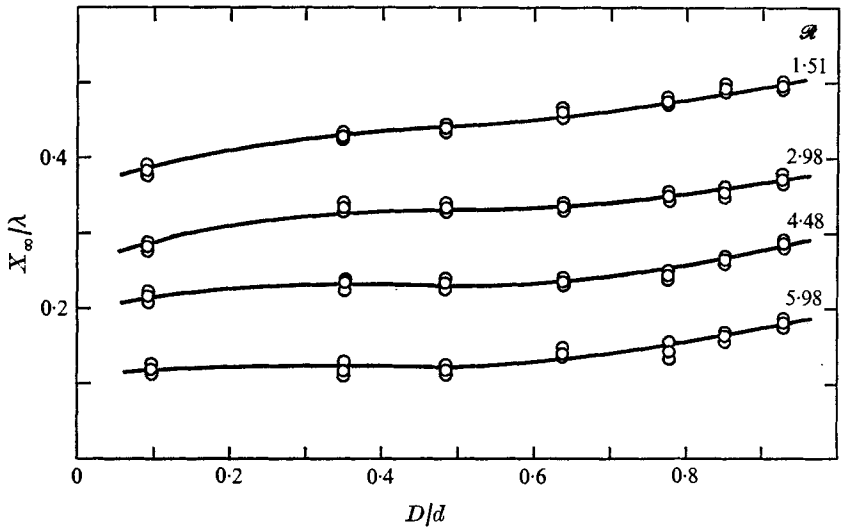

FIGURE 10. Effects of particle size and Reynolds number for wave I. $d/\lambda = 0{\cdot}285$.

channel width. Although the wall pumping patterns, or u/c and v/c on the wall (wave I), for these two figures are the same, the change in wave speed, and thus in $\mathscr{R}$, leads to significant effects on particle transport.

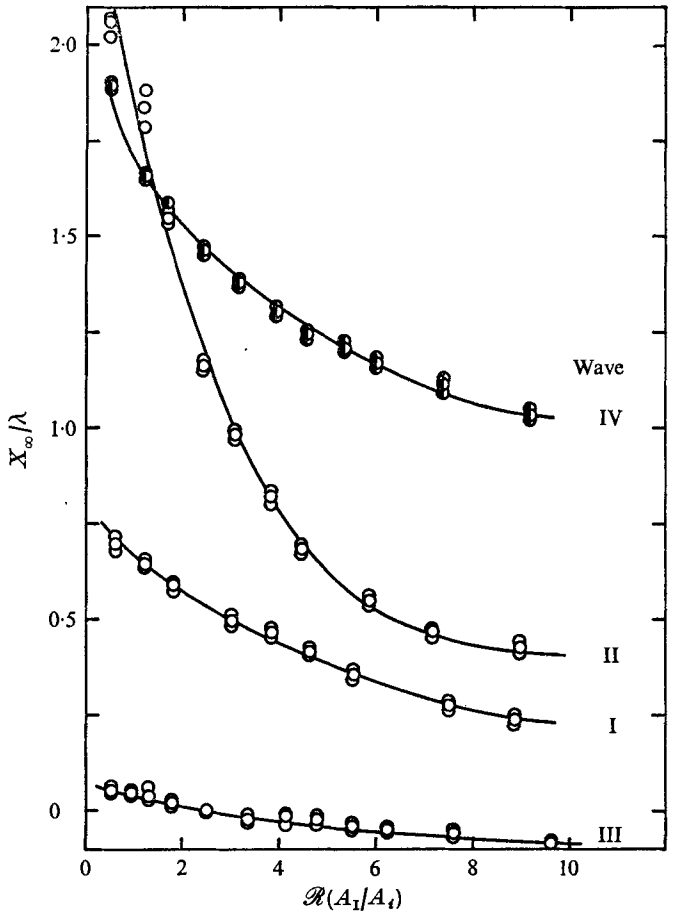

FIGURE 11. Effects of wave amplitude and form on net particle transport. $d/\lambda = 0{\cdot}25$, $D/\lambda = 0{\cdot}10$; A_i denotes amplitude of wave i (i = I–IV).

6. The effects of the amplitude and form of peristalsis

Figure 11 shows a comparison of the net particle transport X_∞/λ in the peristaltic flows for the four different waves. Clearly the pumping action, which can be characterized by the longitudinal momentum flux η per unit depth of the contracting parts of the peristaltic wave (refer to the caption to figure 12), is enhanced by an increased wave amplitude. A decrease in the amplitude may even lead to a net retrograde particle movement at larger Reynolds number.

For waves I, II and III, the pumping action (i.e. contraction and dilatation of the wall) occurs at every section of the bolus. However, in ureteral peristalsis, the pumping in the middle segment of the bolus diminishes because it has become fully dilated, a situation which usually occurs when the bolus is very long. Although this temporarily inactive mid-segment of the bolus does not provide any pumping activity, one cannot immediately conclude that its effect on the particle transport is small. Since, as may be recalled, a positive net force (shown

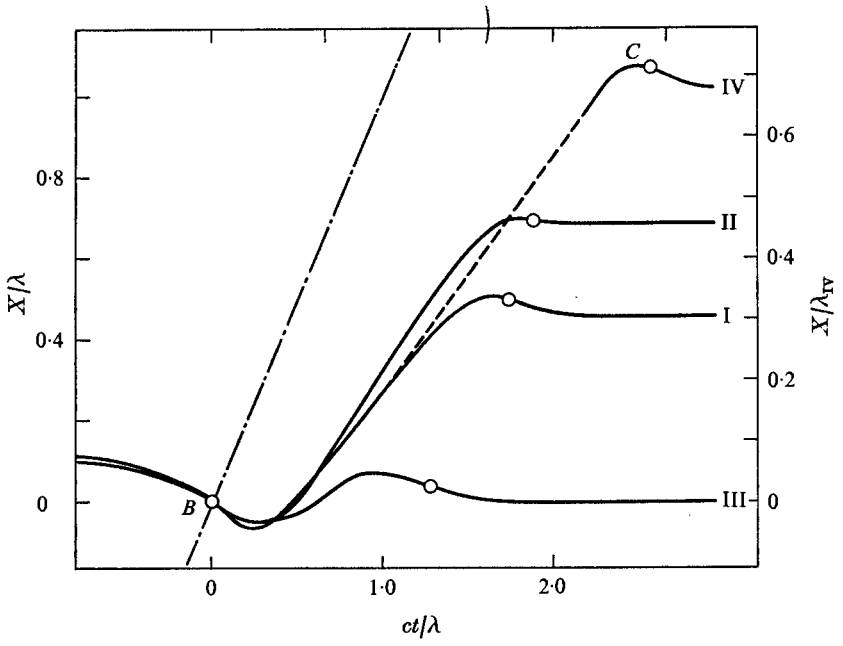

FIGURE 12. Effect of wave amplitude on particle trajectory. $d/\lambda = 0{\cdot}285$, $D/\lambda = 0{\cdot}103$, $\mathscr{R} = 3{\cdot}35$ for wave I; same c for all four waves

Wave	I	II	III	IV
η/η_{I}	1·00	5·74	0·14	1·00
Φ	0·44	0·12	0·02	0·70

in figure 5) acts on the particle when it is within the leading half of the bolus and the force becomes negative in the trailing half, the inactive mid-segment is expected to delay the onset of the negative force. Thus the particle may travel forward with a large velocity when it is in this inactive mid-segment of the bolus. This expectation is confirmed by the experimental results for wave IV (see figure 12). During the mid-portion of the particle motion, the net force acting on it essentially vanishes, thus resulting in a nearly constant particle speed during most of this period, indicated by the dashed-line segment in figure 12. The ratio $X_b/\lambda_{\mathrm{IV}}\,(= X_b/1{\cdot}5\lambda)$ of transport distance to wavelength for wave IV is about 50 % larger than that (X_b/λ) for wave I when $\mathscr{R} = 3{\cdot}35$ and $d/D = 2{\cdot}76$.

7. The effects of longitudinal body force

To explore the mechanics of particle motion by peristalsis along with a longitudinal body force, an experiment was first conducted for particle motion due to a body force alone and then for a body force and peristalsis together. The particle trajectories for these two cases (designated respectively curves 1 and 2 in figure 13) are compared with that (curve 3) for a neutrally buoyant particle pumped by peristalsis. The point O on curve 1 marks the onset of subjection of the particle to a constant longitudinal force $\Delta f = 545$ dynes/cm or

$$[\rho_0 D^3 g(\rho_s - \rho)/\mu^2]^{\frac{1}{2}} = 8{\cdot}7,$$

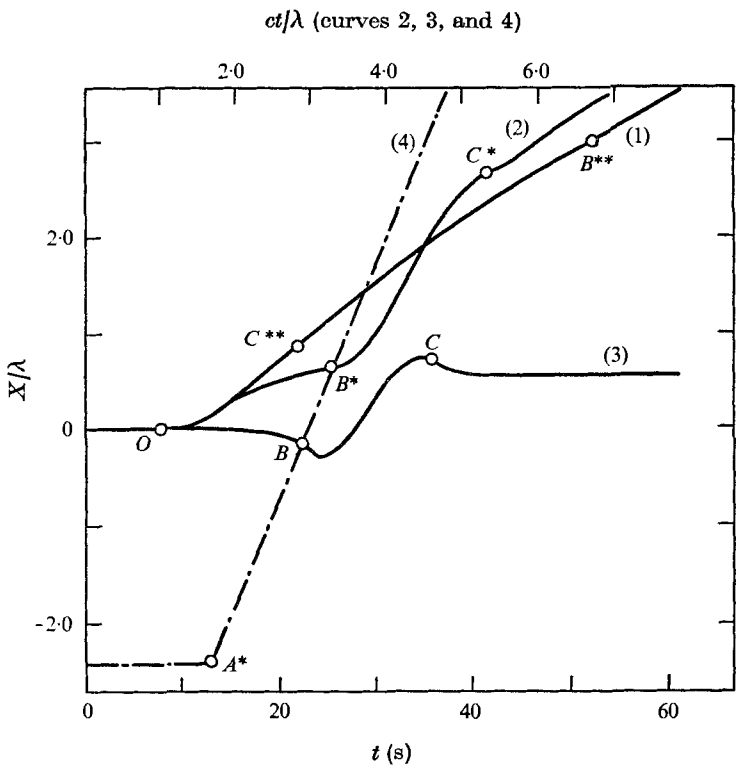

FIGURE 13. Comparison of particle motions due to a body force, peristalsis or both. Wave I, $\mathscr{R} = 4{\cdot}01$, $d/\lambda = 0{\cdot}285$, $D/\lambda = 0{\cdot}103$, $\mathscr{F}/\mathscr{R} = 8{\cdot}69$.

resulting in the forward movement of the particle. The peristaltic wave begins to propagate downstream (to the right) from point A^*. At this instant, the leading edge of the wave is a distance X_0 behind the particle. The trajectory of the leading edge is shown by the dashed straight line (4) in the figure. Also labelled along curve 2 are points B^* and C^*, which signify the overtaking of the particle by the leading and trailing edges, respectively, of the bolus. Without the longitudinal body force, these two points would coincide with points B and C on curve 3, which was produced by peristalsis alone. The effects of the leading and trailing edges on the particle velocity (i.e. the slope of the particle trajectory) for curve 3 can be seen also on either side of B^* and C^* for curve 2. Because the effects of the body force dominate those of the peristalsis in this case, no local retrograde motion is observed. The marked increase in the particle velocity between B^* and C^* results in a 130 % increase in X_b (the transport distance per bolus).

The terminal velocity of a particle moving between two parallel walls measured in this study has been compared with the theoretical and experimental data discussed by Happel & Brenner (1965, p. 344). Owing to the pulley friction and viscous drag on the thread, the present particle velocities are about 10 % smaller than those predicted by Faxén's theory. The disagreement is smaller than the scatter ($\pm$ 15 %) of Jones & Kundsen's (1961) experimental data for a sphere or cylinder towed in a tube. A particle moving through a stationary bolus owing to a

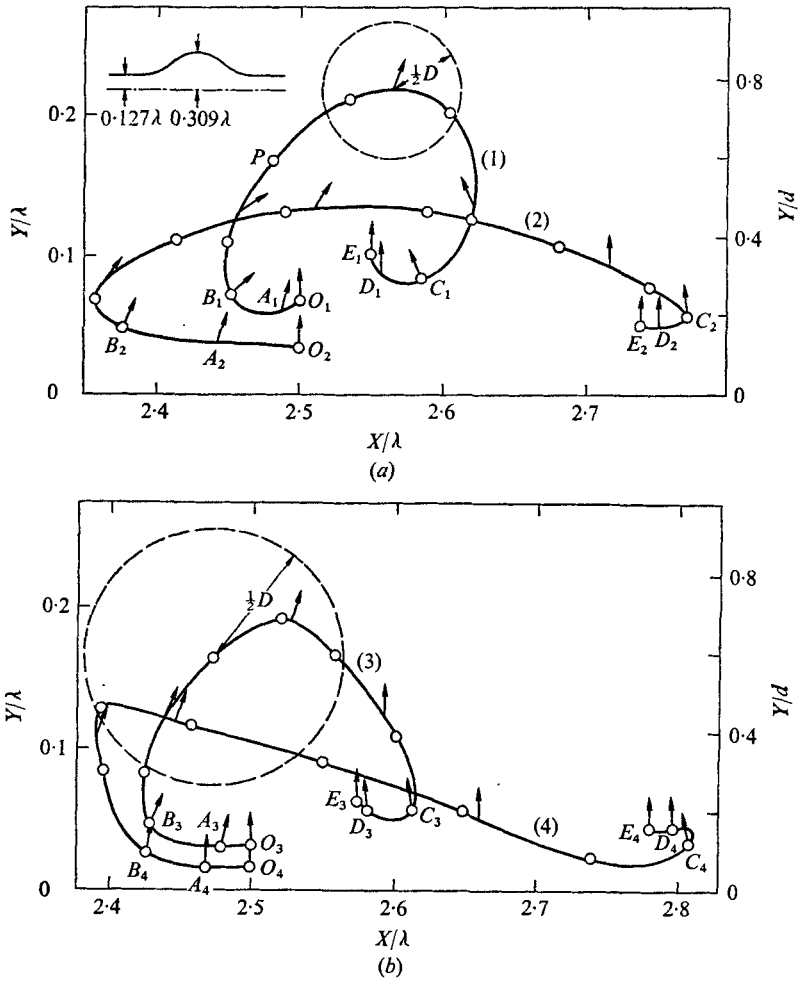

FIGURES 14(a, b). For legend see facing page.

forward body force Δf will pass the trailing edge (at point C^{**} on curve 1) first and then the leading edge (point B^{**}). The practically constant velocity over this period suggests that the transient effects of the curved wall offset the reduction in boundary effects associated with the increase in the spacing between the walls.

8. Lateral eccentric effects

A continuous decrease in X_∞ is found as the particle's initial position is progressively offset from the symmetry plane of the peristaltic wave. As shown in figure 14(a), a circular particle with $D/d = 0{\cdot}36$ initially positioned at $X_0/\lambda = 2{\cdot}5$ and $Y_0/d = 0{\cdot}235$ experiences a clockwise (refer to case 1) rotation followed first by a counter-clockwise one and then by a clockwise rotation. With an initial particle orientation indicated by a vertical arrow at O, the rotation of a circular particle along the trajectory is shown by the directional vector at various positions

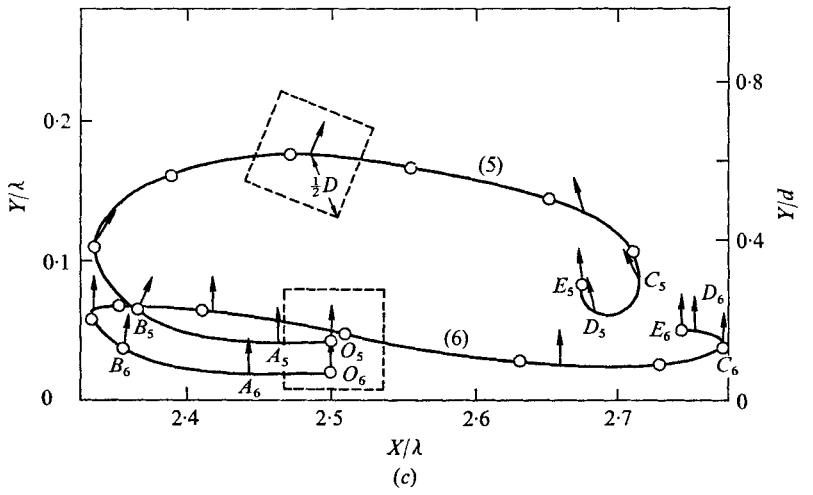

FIGURE 14. Particle trajectories with lateral excursions. Wave I, $\mathscr{R} = 4{\cdot}30$, $d/\lambda = 0{\cdot}252$. (*a*) $D/\lambda = 0{\cdot}103$. (*b*) $D/\lambda = 0{\cdot}186$. (*c*) $D/\lambda = 0{\cdot}103$.

Curve	$c\Delta t/\lambda$	$c(t_A - t_O)/\lambda$	$c(t_B - t_A)/\lambda$	$c(t_D - t_C)/\lambda$	$c(t_E - t_D)/\lambda$
1	0·19	0·48	0·47	0·49	0·50
2	0·20	0·44	0·43	0·48	0·50
3	0·19	0·47	0·46	0·48	0·49
4	0·21	0·46	0·45	0·46	0·49
5	0·22	0·44	0·41	0·47	0·49
6	0·20	0·42	0·39	0·49	0·50

of the particle relative to the wave, $X^*/\lambda = 2{\cdot}5$, $1{\cdot}5$, $1{\cdot}0$, $0{\cdot}75$, $0{\cdot}5$, $0{\cdot}25$, 0, $-0{\cdot}5$ and $-1{\cdot}0$, corresponding to the consecutive arrows (from O to E) along the path. The reader may want to refer to the sketch of the wavy wall in figure 2 to visualize these various positions of X^*/λ. As defined in figure 5, the points B and C denote respectively the leading and the trailing edges of the wave passing the centre of the particle. The speed of the particle translation within the bolus can be deduced from the pathline segments between two adjacent open circles separated by equal time increments $c\,\Delta t/\lambda$. The particle transit times from O to A, A to B, C to D and D to E (the subscript 1 indicating case 1) are somewhat longer than the aforementioned increment; they are also listed in the caption to figure 14. At each of these points (in the fixed frame), one can easily calculate the exact position of the wavy walls from these time increments and the data for d/λ, A/λ and D/λ. For example, when the particle centre is at P in case 1, the leading edge of the wall will be located at $X/\lambda = 2{\cdot}45 + 2c\Delta t/\lambda = 2{\cdot}87$, $Y/\lambda = 0{\cdot}5d/\lambda = 0{\cdot}127$. For the same particle, the asymmetric effects on the particle transport by peristalsis for case 1 are compared with those for case 2. The conditions for these two peristaltic flows are the same except for the initial lateral positions Y_0/λ of the particle. As Y_0/λ reduces, both the lateral oscillation and rotation decrease while the longitudinal motion increases. For these two cases the particle comes to rest practically at its original orientation. The net longitudinal displacement for case 1 is about one-fifth of that for a symmetric case (i.e. $Y_0/d = Y/d = 0$).

The particle trajectories shown in figures 14 (*b*) and (*c*) (cases 3–6) were obtained

from the same peristaltic wave (wave I) as those in figure 14(*a*). However, cases 3 and 4 are for a larger circular particle with $D/d = 0{\cdot}652$ as compared with 0·36 for cases 1 and 2. Although the initial eccentricities (i.e. the values of Y_0/d) for cases 3 and 2 are about the same, a larger lateral excursion for case 3 is caused by the bigger size of the particle, which results in the relatively larger deviation in the gaps on either side of the particle. For example, the initial gap between the wall and the particle is $0{\cdot}11d$ for case 3 and $0{\cdot}17d$ for case 2. Figure 14(*c*) shows the trajectories of two particles of square cross-section. The diagonal dimension is the same as the particle diameter for cases 1 and 2. The initial orientations of these particles are also shown in this figure. The results show that, for $Y_0/\lambda = 0{\cdot}04$, the shape of the trajectory for a square particle follows the trend of the change in shape of the trajectories between cases 1 and 2. Although the representative data shown in figure 14 do not give a complete quantitative measure of the effects of the particle size D/d and the initial orientation of a square particle on the particle transport, they do indicate the following.

(i) Large lateral swing and rotation of the particle are associated with large eccentricity Y_0/d.

(ii) The sensitivity of the particle trajectory to Y_0/d increases with D/d.

(iii) The effects of the shape of the particle on its motion are much smaller than those of its diameter and of Y_0/d.

(iv) A significant reduction in the net longitudinal transport per peristalsis occurs when Y_0/λ is greater than approximately 0·04.

The experimental data on the particle's lateral migration when it is pumped by wave IV indicate that it migrates towards the wall, following a trajectory similar to those for pumping by wave I. Besides increasing X_∞, the effects of the mid-segment on an off-centre particle are also to cause a net rotation and lateral migration of the particle. The rotation of the particle in the mid-segment is somewhat similar to the rotation of a particle in a tube; that is, the particle rotation causes a decrease in the fluid velocity near the side wall for Poiseuille flow.

More complicated motion will occur when the particle is subjected to a body force with a significant lateral component. In this situation, the particle is expected to move towards and even to lean on the wall, resulting in ineffective particle transport analogous to the process of calculus movement in a ureter.

9. Interaction of particle and fluid

In order to explore further the fluid–particle interaction, a series of flow patterns was obtained both with and without the particle. In figure 15(*a*) (plate 2), one can see the symmetric flow pattern (with respect to the longitudinal axis) as well as the small variation in velocity in the core region of the bolus. The velocity vectors at various points of the field can be measured from the pathline segments, as shown in figure 6(*b*). Because of the small values of $\partial u/\partial y$ in the core region, the presence of a small particle there (see figure 15*b*) does not lead to a noticeable disturbance to the flow field, even though the particle is slightly off the symmetry axis and is square in shape.

Small velocity variations in the core region can be seen also in figure 16(*a*) (plate 2), which was photographed in the moving frame. In this case, $d/\lambda(=0{\cdot}13)$ is much smaller than that (0·25) in the previous figure. The small velocity in the core indicates the beginning of the trapping (i.e. a small mass of fluid moving with the wave) which has been pointed out by Shapiro *et al.* (1969) for a linear case ($A \ll \lambda$). For a small circular particle moving with the bolus (see figure 16*b*), only the flow field around the leading (right-hand) end of the particle shows a slight deviation from the corresponding no-particle case. With a further decrease in d/λ, the trapping region forms a pair of vortices; since these vortices will not be observed in the fixed frame, they are, in fact, the secondary flow viewed in the moving frame. Thus the presence of a small square particle between these two vortices in figure 17 (*b*) (plate 3) is not responsible for their formation. That is to say, the secondary flow observed in the moving frame does not necessarily represent boundary-layer separation. Should a study of separation for large Reynolds number be conducted, the camera would travel with the velocity of the moving particle rather than with the speed of the peristalsis. Figure 18 (plate 3) exhibits the flow patterns when a particle moves away from the symmetry axis. The streamlines near the other side of the channel appear to be similar to those for the corresponding no-particle case. The undistorted straight streamline along the axis further indicates that the presence of the particle does not lead to a significant disturbance to the flow field.

The particle trajectories shown in curves 1 and 4 of figure 14 are also plotted in figure 19 (plate 3) so as to provide a view of the particle motion in the moving co-ordinates. The velocity of the particle can be deduced from the spacing between the circular points, which correspond to those in figure 14. Also shown in figure 19 are the fluid streamlines (solid lines) in the wave frame for cases without the particle. The particle trajectory (indicated by the dashed line) deviates noticeably from the corresponding pathline (solid line) of fluid for the no-particle case; the latter passes through the position of the particle at the leading edge of the bolus. The bundle of streamlines for the no-particle case diverges and then converges and may even conceive a pair of secondary vortices when d/A is small.

A slight migration of the particle away from the axis is found for the asymmetric case, and is attributed primarily to inertial effects. It seems that the effects of the unsteadiness of the particle motion are smaller than the effects of the curvilinear flow characteristics. The present results for a neutrally buoyant particle migrating outward in a curvilinear flow appear to be analogous to those for a dilute suspension in plasma of neutrally buoyant red blood cells in the laminar vortex observed recently by Goldsmith & Karino (private communication). For the case of peristaltic flow, the lateral migration implies that the longitudinal transport of the particle per bolus will progressively decrease for subsequent peristalsis.

The authors would like to express their appreciation to Dr Ting-Cheng Hung of Washington University for his suggestions on the experimental method of generating the peristaltic waves and to Miss Nancy Motley for her secretarial assistance. T. D. B. was supported by NIH Training Grant GMO 1455 and T.-K. H. by NSF Grant GK 31514 and NIH Grant HL-12714.

REFERENCES

BARTON, C. & RAYNOR, S. 1968 Peristaltic flow in tubes. *Bull. Math. Biophys.* **30**, 663–680.

BOYARSKY, S., GOTTSCHALK, C. W., TANAGHO, E. A. & ZIMSKIND, P. D. (eds) 1971 *Urodynamics*. Academic.

BUNGAY, P. & BRENNER, H. 1973 Pressure drop due to the motion of a sphere near the wall bounding a Poiseuille flow. *J. Fluid Mech.* **60**, 81–96.

BURNS, J. C. & PARKES, T. 1967 Peristaltic motion. *J. Fluid Mech.* **29**, 731–743.

FITZ-GERALD, J. M. 1972 Mechanics of red-cell motion through very narrow capillaries. *Proc. Roy. Soc.* B **174**, 193–227.

FOX, M., PYRAH, L. N. & RAPER, F. P. 1965 Management of ureteric stone: a review of 292 cases. *Brit. J. Urol.* **37**, 660–670.

FUNG, Y. C. 1971 Peristaltic pumping: a bioengineering model. In *Urodynamics* (ed. S. Boyarsky *et al.*), pp. 178–198. Academic.

FUNG, Y. C. & YIH, C. S. 1968 Peristaltic transport. *J. Appl. Mech.* **35**, 669–675.

GOLDSMITH, H. L. & MASON, S. G. 1966 In *Rheology: Theory and Application* (ed. F. R. Eirich), vol. 4, pp. 85–250. Academic.

HAPPEL, J. & BRENNER, H. 1965 *Low Reynolds Number Hydrodynamics*. Prentice-Hall.

JAFFRIN, M. Y. 1971 Inertia and streamline curvature effects on peristaltic pumping. *Int. J. Engng Sci.* **11**, 681–699.

JONES, A. M. & KNUDSEN, J. G. 1961 Drag coefficients at low Reynolds numbers for flow past immersed bodies. *A.I.Ch.E.J.* **7**, 20–25.

KIM, H. L., LABAY, P., BOYARSKY, S. & GLENN, J. F. 1970 An experimental model of ureteral colic. *J. Urol.* **104**, 380–391.

LABAY, P. C. & BOYARSKY, S. 1971 Ureteral peristaltic pressure methods. In *Urodynamics*, (ed. S. Boyarsky *et al.*). Academic.

LEW, H. S., FUNG, Y. C. & LOWENSTEIN, C. B. 1971 Peristaltic carrying and mixing of chyme in the small intestine. *J. Biomech.* **4**, 297–315.

LI, C. H. 1970 Peristaltic transport in circular cylindrical tubes. *J. Biomech.* **3**, 513–523.

LIGHTHILL, M. J. 1968 Pressure-forcing of tightly fitting pellets along fluid-filled elastic tubes. *J. Fluid Mech.* **34**, 113–143.

LYKOUDIS, P. S. & ROOS, R. 1970 The fluid mechanics of the ureter from a lubrication point of view. *J. Fluid Mech.* **43**, 661–674.

ROUSE, H. & MACAGNO, E. O. 1966 On the use of models in fluids research. In *Hemorheology* (ed. A. L. Copley), pp. 231–236. Pergamon.

SHAPIRO, A. H. 1967 Pumping and retrograde diffusion in peristaltic waves. *Proc. Workshop Ureteral Reflux Children, Nat. Acad. Sci., Wash.*

SHAPIRO, A. H., JAFFRIN, M. Y. & WEINBERG, S. L. 1969 Peristaltic pumping with long wavelengths at low Reynolds number. *J. Fluid Mech.* **37**, 799–825.

SKALAK, R., CHEN, P. H. & CHIEN, S. 1973 Effect of hematocrit and rouleaux on apparent viscosity in capillaries. *Biorheol.* **9**, 67–87.

TAYLOR, G. I. 1951 Analysis of the swimming of microscopic organisms. *Proc. Roy. Soc.* A **209**, 447–461.

TONG, P. & VAWTER, D. 1972 An analysis of peristaltic pumping. *J. Appl. Mech.* **39**, 857–862.

WANG, H. & SKALAK, R. 1970 Viscous flow in a cylindrical tube containing a line of spherical particles. *J. Fluid Mech.* **38**, 75–96.

YIN, F. C. P. & FUNG, Y. C. 1969 Peristaltic waves in circular cylindrical tubes. *J. Appl. Mech.* **36**, 579–587.

YIN, F. C. P. & FUNG, Y. C. 1971 Comparison of theory and experiment in peristaltic transport. *J. Fluid Mech.* **47**, 93–112.

ZIEN, T. F. & OSTRACH, S. 1970 A long wave approximation to peristaltic motion. *J. Biomech.* **3**, 63–75.

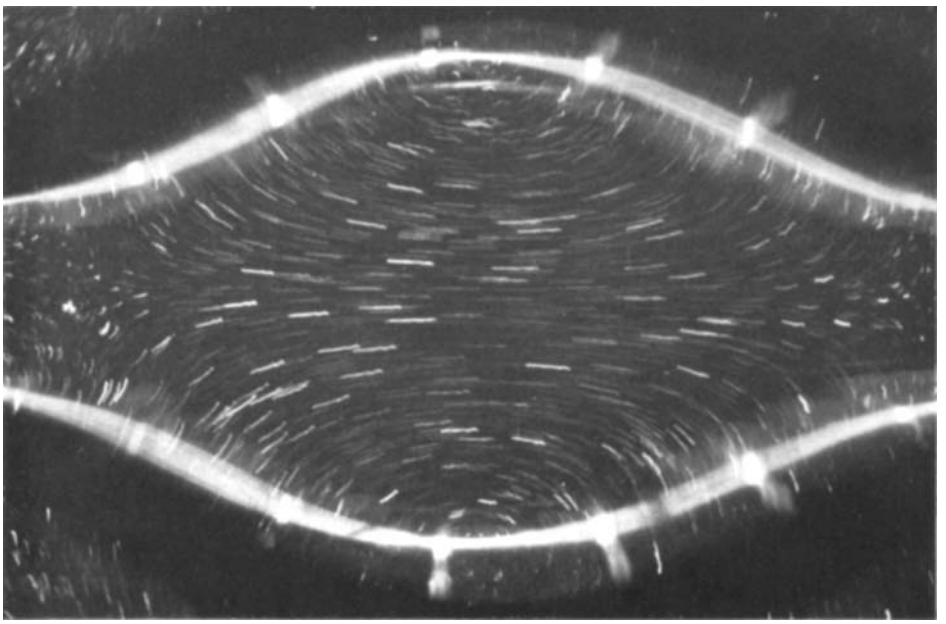

(*a*)

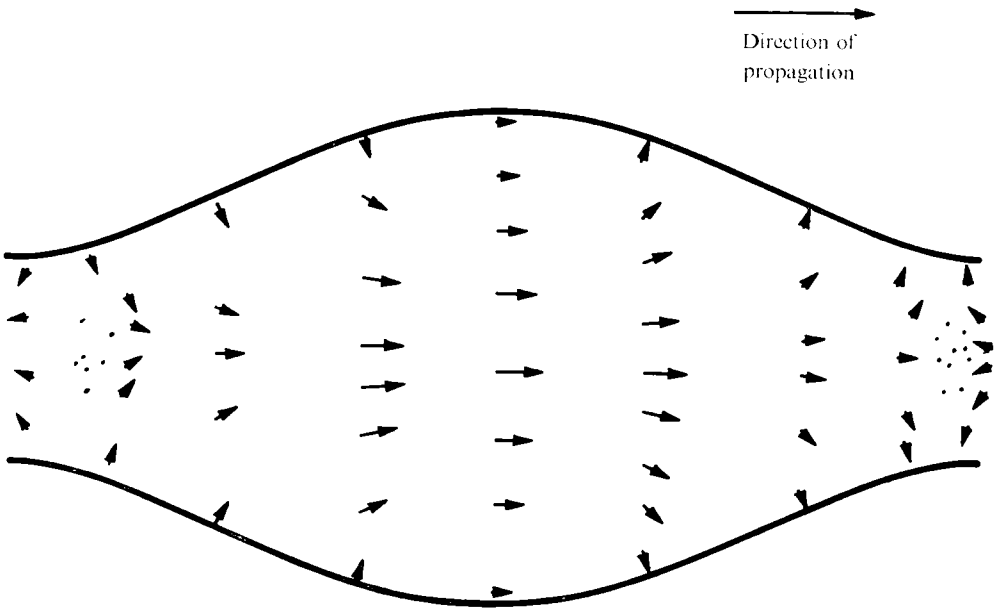

(*b*)

FIGURE 6. (*a*) Flow pattern observed from the fixed reference frame.
(*b*) Velocity distribution. Wave I, $\mathscr{R} = 2{\cdot}4$, $d/\lambda = 0{\cdot}21$.

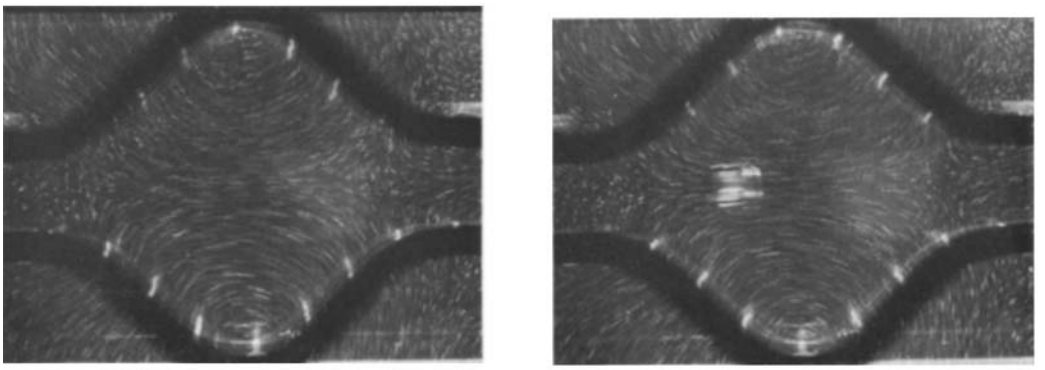

(*a*) (*b*)

FIGURE 15. Flow patterns recorded in the fixed frame. Wave II, $\mathscr{R} = 6{\cdot}28$, $d/\lambda = 0{\cdot}245$. (*a*) No particle. (*b*) $D/\lambda = 0{\cdot}103$.

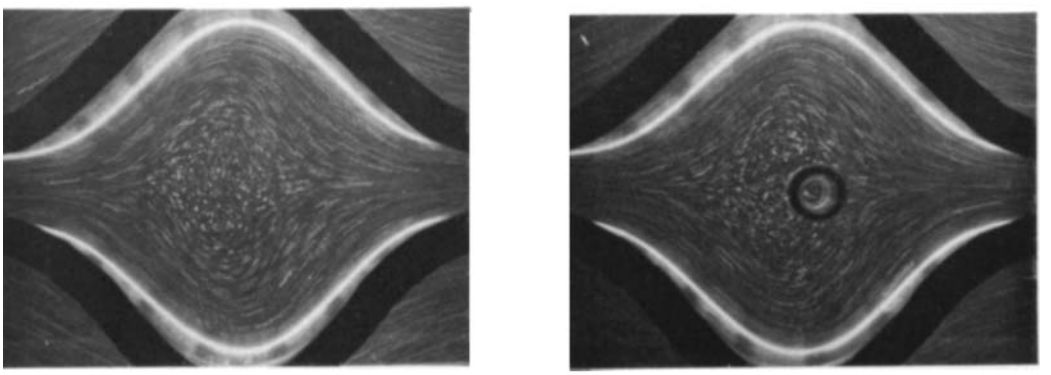

(*a*) (*b*)

FIGURE 16. Flow patterns recorded in the moving frame showing incipient trapping. Wave II, $\mathscr{R} = 6{\cdot}28$, $d/\lambda = 0{\cdot}31$. (*a*) No particle. (*b*) $D/\lambda = 0{\cdot}103$.

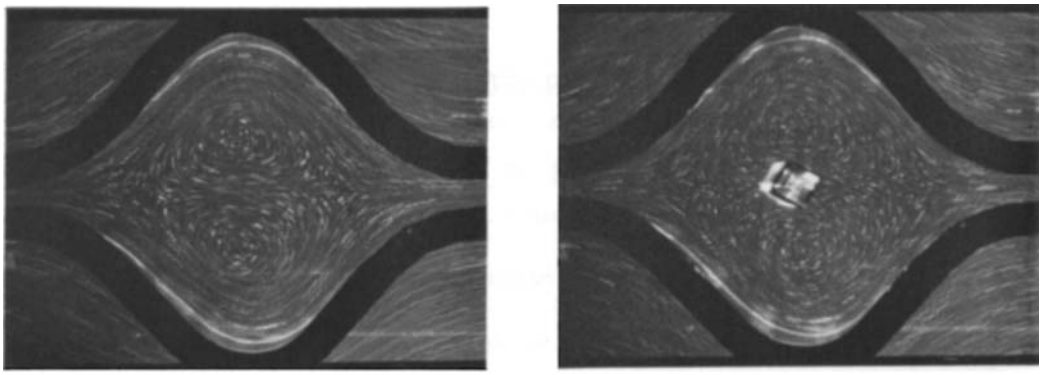

(*a*) (*b*)

FIGURE 17. Secondary vortices in the moving frame. Wave II, $\mathscr{R} = 6{\cdot}28$, $d/\lambda = 0{\cdot}095$. (*a*) No particle. (*b*) $D/\lambda = 0{\cdot}103$.

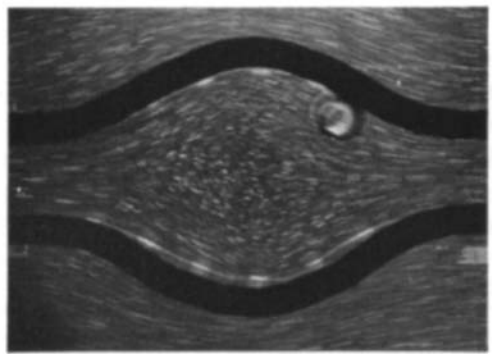

FIGURE 18. Flow pattern with a particle near the wall. Wave I, $\mathscr{R} = 4{\cdot}30$, $d/\lambda = 0{\cdot}252$, $D/\lambda = 0{\cdot}103$.

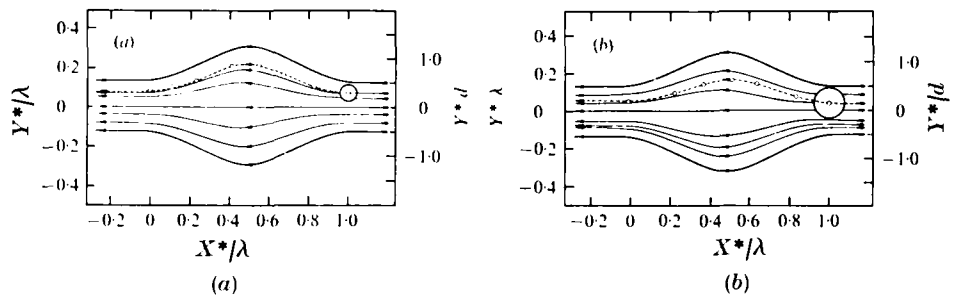

(*a*) (*b*)

FIGURE 19. Comparison of particle trajectory with the streamlines (moving frame) for the no-particle case. Wave I, $\mathscr{R} = 4{\cdot}30$, $d/\lambda = 0{\cdot}252$. (*a*) $D/\lambda = 0{\cdot}103$. (*b*) $D/\lambda = 0{\cdot}186$.